Supplementary Information

Torsionally broken symmetry assists infrared excitation of biomimetic charge-coupled nuclear motions in the electronic ground state

A. Simulation protocol for the trajectory calculations

A1. Generating the thermal population:

The very first step in the simulations is the construction of the DASPMI molecule in the gas phase, optimised at the second-order Møller-Plesset level [1,2] with 6-31G* Pople basis set (MP2/6-31G*), using implicit dichloromethane as the solvent under the Polarizable Continuous Model (PCM) [3], employing the GAUSSIAN computer package [4]. The optimised chromophore is then embedded in the centre of a cubic box of size 60 x 60 x 60 Å, containing a total of 1648 dichloromethane (DCM) solvent molecules. The chromophore is kept frozen and the solvent system is minimised at the molecular mechanics (MM) level, using the conjugate-gradient method with periodic boundary conditions. The nuclear charges of the chromophore atoms for this purpose are calculated using the Second Order Electrostatic Potential Fitting Method (ESPF) at the MP2/6-31G* level. The binding and van der Waals parameters are taken from the OPLS_aa force field [5]. The minimised chromophore-solvent system is then relaxed using a 5000 ps long molecular dynamics (MD) simulation under the isothermal-isobaric ensemble (NPT), set at 1 atm of pressure and 298 K of temperature using the GROMACS software package [6]. During the first 300 ps of the simulation, the system gradually thermalises to 298 K, equilibrates for the next 700 ps and relaxes for the next 4000 ps (Fig. S6). From this dynamic simulation step, named production, snapshots are extracted every 10 ps, involving a 20-Å solvent layer (544 DCM molecules) to complete a full set of 400 configurations in order to define the hybrid quantum mechanics / molecular mechanics (QM/MM) model. In this model, the chromophore is treated at the QM level using the 2-root-state-average complete active space self-consistent field (CASSCF) method with a 6-31G* base set and an active space comprising 12 electrons in 11 orbitals (CASSCF/631-G*/12,11). The solvent molecules, located at 4 Å from any chromophore atom, are treated at the MM level (OPLS_aa force field) and are allowed to move during the QM/MM molecular dynamics, while the rest of the solvent group remain frozen. The QM/MM dynamics is computed following a 2-root-state-average CASSCF gradient for 200 fs with a time step of 1 fs (41.3 au) to generate a Boltzmann-like thermal population in the electronic ground state (S_0), which is considered to be the "initial conditions". The 2-ps long S_0 and the short excited-state (S_1) dynamics are computed following the same level, 2-root-state average CASSCF/ 6-31G*/OPLS-aa. The temporal evolution of the S_0-S_1 electronic parameters (namely, oscillator strength, energy gap, and charge difference) along the trajectories is computed every 10 fs by subsequent single-point 3-root-state-average CASPT2/6-31G*/OPLS-aa calculations, which provide a more quantitative evaluation. All QM/MM calculations are carried out using the Molcas/Tinker packages [7,8].

A2. Generating the vibrationally-excited ground-state population

The thermalised population in S_0 is subsequently projected onto S_1, while conserving positions and momenta. Following S_1 relaxation for 15 fs, the population is projected back onto S_0. This is because for linear π-delocalised systems like conjugated polyenes, it is known [9] that the bond-length alternation (BLA) stretching mode is activated (with a period of ~15 fs) during the S_1 relaxation from the Franck-Condon region. Consequently, a snapshot of the S_1 population after 15 fs, when projected onto S_0, is expected to result in a vibrationally-excited S_0 population with energy funneled into the BLA stretching mode. This population represents the initial conditions for studying the S_0 vibrational dynamics for the following 2 ps (Fig. 4), which constitutes the very premise of our key observations.

B. Survey of the initial conditions

Here, we enumerate the various calculations performed to examine the role of BLA at every intermediate simulation step leading up to the initial conditions — namely, the creation of a vibrationally-excited BLA-activated S_0 population. Our first aim is to identify the S_0 normal mode associated with the pronounced BLA motion localised at the central ethylenic bridge. This requires S_0 optimisation of a selected geometry. The evolution of this optimised geometry may then be traced and visually inspected at every simulation step. Notably, the geometry optimisation erases all thermal information. This treatment is markedly different from the trajectory calculations, which include temperature-related effects originating from the creation of the initial thermal S_0 population, as described above. However, a comparison between the evolution of the optimised geometry and the trajectories representing the entire population illustrates quantitative differences in a qualitatively unanimous and consistent picture. This justifies the methodology adopted here, which facilitates visual inspection of the evolved geometries and provides valuable insight into the induction of BLA character.

In order to select a geometry for the S_0 optimisation, the geometry corresponding to the peak of the simulated absorption spectrum for the thermal S_0 population (see Fig. S7A for further details) is considered, since it is representative of the average of the total population. Following the geometry optimisation at the 2-root-state-average CASSCF/6-31G* (including the effect of the solvent-shell configuration), a vibrational frequency analysis reveals an intense spectral peak localized at 1796 cm^{-1} (Fig. S8A). The corresponding normal mode is characterised by a distinct BLA motion of the skeletal structure, particularly in the region surrounding the central ethylenic bridge (Fig. S8C). Incorporating the correctional factor of 0.9 associated with the intrinsic overestimation of the computed frequencies due to the simulation framework employed, the frequency of this normal mode translates to 1616 cm^{-1}. This is close to the experimental value of 1577 cm^{-1} in the steady-state infrared absorption spectrum of DASPMI in dichloromethane (Fig. 1B), representing the S_0 vibrational mode excited by the mid-infrared pump laser in the experiment.

For the purpose of comparison, the selected geometry is also optimised on S_1. The normal mode of interest, with conspicuous BLA character around the central ethylenic bridge (Fig. S8D), now corresponds to an intense spectral peak at 1173 cm^{-1} (Fig. S8B).

Our next aim is to demonstrate the validity of our hypothesis that the BLA stretching mode is activated during the S_1 relaxation from the Franck-Condon region. To this end, ten randomly selected trajectories from the entire population of 400 trajectories are analysed and visually inspected, using the Visual Molecular Dynamics (VMD) software. The trajectories clearly depict temporal oscillations along the BLA coordinate (Fig. S9), thereby confirming that energy is released into the BLA mode. This behaviour is qualitatively reproduced (Fig. S9) by the Franck-Condon relaxation trajectory, arising from the vertical transition of the selected S_0-optimised equilibrium geometry to the Franck-Condon point on S_1. This facilitates a visual representation of the direction along which the Franck-Condon relaxation occurs (Fig. S10A), which may immediately be compared with the normal-mode representation in S_0 (Fig. S8C) or S_1 (Fig. S8D).

The final aim is to characterise the initial conditions, particularly in terms of the energy injected into the BLA mode, which actuates the ensuing S_0 vibrational dynamics (Fig. 4). Following projection back onto S_0, the selected geometry is further relaxed for 20 fs, divided into 5-fs segments in order to compute the displacement vectors. The average displacement vector (Fig. S10B) is then compared with the S_0 normal-mode vector (Fig. S8C). The relative orientation of the two vectors (computed by the scalar product) reveals a parallelism of 35%. This is indicative of the percentage of the total vibrational energy released into the BLA mode, where the total vibrational energy is the sum of the vibrational energies in S_0 and S_1 and is ~36 kcal/mol for this selected geometry. Considering the 35% parallelism, ~13 kcal/mol is therefore estimated to be released into the BLA mode. This is validated by a computation of the BLA energy in the harmonic approximation, which also yields a value of 13 kcal/mol. As discussed previously, this analysis is qualitative, since it does not incorporate any thermal effects. The vibrational energy injected into the experimentally relevant BLA mode is ~7 kcal/mol. This value is computed from the hessian at the turning points of the classical trajectories, and averaged over the entire population of 400 trajectories. The discrepancy with the experimental value (~5 kcal/mol) is within acceptable limits, given the simulation protocol generates classical trajectories, which do not produce quantised vibrational motion. Furthermore, the simulations consider a fully anharmonic model with 105 vibrational degrees of freedom for the DASPMI molecule and hundreds of degrees of freedom for the solvent molecules. On calculating the energy for the first vibrationally-excited level in S_0 along this particular BLA mode in the harmonic approximation, it may be surmised that vibrational-ladder climbing up to the first vibrationally-excited level in S_0 may have been achieved in the course of the simulations. The zero-point-energy (ZPE) contributions associated with the trajectory vibrational modes are also evaluated. As documented in Table S2, the maximum ZPE corresponding to the highest frequency vibrational mode is less than 30% of the vibrational energy initially injected into the experimentally relevant BLA mode. Besides, the lowest α vibrational component (that appears to be the one associated with the experimentally observed oscillations) features a small 0.1 kcal/mol ZPE.

C. Ground-state vibrational dynamics

Following the creation of the vibrationally-excited S_0 population with the BLA stretching mode activated, the ensuing vibrational dynamics is simulated at the 2-root-state-average CASSCF level for 2 ps (Fig. 4). The time-evolution of the oscillator strength, f, the energy gap, E, and the charge difference, q, between S_0 and S_1 show distinct peaks at 1250 cm^{-1} and in the vicinity of 50 cm^{-1} in the Fourier domain (Fig. 4). This may be correlated to the time-evolution of the C_2-C_3=C_4-C_5 dihedral, α, the H-C_3=C_4-H dihedral, β, the π-overlap, τ, and the BLA (Fig. 3).

The vibrationally-excited S_0 population reveals that the ethylenic stretching incorporated in the activated BLA stretching mode can effectively couple with the ethylenic torsional mode, as it alters the ethylenic π-bonding character, and therefore the vibronic coupling. Thus, the coupling between BLA and α is expected in a situation where it is not prevented by symmetry. This is independently examined by calculating the sensitivity of the S_0-S_1 energy gap with respect to all the vibrationally populated modes resulting from the simulation (Table S1). The 1475 cm^{-1} mode (corresponding to the C-C-H bending of the ethylenic bridge), and the 1300 cm^{-1} mode (corresponding to the C-N stretching) have little influence on the π-overlap, and therefore the S_0-S_1 energy gap (6% and 14%, respectively). On the contrary, the experimentally relevant 1796 cm^{-1} mode (corresponding to the bridge-localised stretching BLA mode) changes the energy gap up to 28%. This assignment appears to be logical while considering the change in the overlap of the orbitals describing the π-bonding character. In contrast with the other modes, both stretching and torsion along the ethylenic bridge effectively change the π-overlap (Table S1). Furthermore, the sensitivity of the S_0-S_1 energy gap is also examined with respect to:

1. the geometrical changes along the experimentally relevant 1796 cm^{-1} mode for a suitably selected geometry representing the thermalised population;

2. the geometrical changes induced by the simulation protocol, relaxing the same representative structure in S_1.

The result shows that 1 and 2 generate the same energy gap sensitivity (the change in the S_0-S_1 energy gap being 46 and 49 kcal/mol, respectively). This supports the fact that our simulation protocol, involving projection onto S_1 and subsequent relaxation onto S_0, is equivalent to distorting a thermalised geometry in equilibrium along the experimentally relevant vibrational mode.

D. Potential-energy surface mapping

In order to locate the conical intersection, the Franck-Condon geometry, arising from the vertical transition of the selected S_0-optimised equilibrium geometry, is gradually twisted in the course of several constrained optimisations. The torsional angle, α, representing the C_2-C_3=C_4-C_5 dihedral along the central ethylenic bridge, is decreased from 177^0 for the Franck-Condon geometry to 130^0. This is followed by

structural relaxation until convergence to a geometry with near-zero energy difference between S_0 and S_1. From the optimised conical-intersection geometry (Fig. S11A), the local vectors, g and h, spanning the branching plane around the conical intersection point are extracted and identified as BLA and α, respectively. These parameters serve as the coordinates along which the S_0 (Fig. S12A) and S_1 (Fig. S12B) potential energy surfaces are mapped in the vicinity of the conical intersection point (Fig. S12D).

An analysis of the charge-transfer character is subsequently performed on S_0 in order to distinguish between the diradical (or covalent) region and the charge-transfer region, separated by the conical intersection point (Fig. S12C). The S_0-optimised geometry is characterised by a positive charge localised on the acceptor, which is diminished in the S_0 charge-transfer region. The charge-transfer character, quantified by the partial charge, ρ, localised on the acceptor is attenuated from a value close to unity in the diradical region to a value close to zero in the charge-transfer region along the BLA coordinate (Fig. S12C). The corresponding transition-state geometries, TS_{dir} (Fig. S11B) and TS_{CT} (Fig. 6C), are determined initially (as a first approximation) by constrained optimisations, fixing the parameter α and varying the BLA, followed by subsequent TS optimisation (without constraints) to find the final TS geometry. Notably, TS_{CT} provides a lower energy barrier (by approximately 10 kcal/mol) compared to TS_{dir}.

To establish the minimum-energy path, two geometries with $\Delta\alpha = \pm 5^0$, compared to $\alpha = 91^0$ for TS_{CT}, are selected as starting points to administer paths towards the reactant trans (Fig. 6A) and product cis (Fig. 6D) isomer states. The minimum-energy path along with the corresponding variation in ρ may then be traced in the parameter space defined by BLA and α (Fig. S13 and Fig. 5B). The substantial change in the Mulliken charge distribution is also shown (Fig. S14).
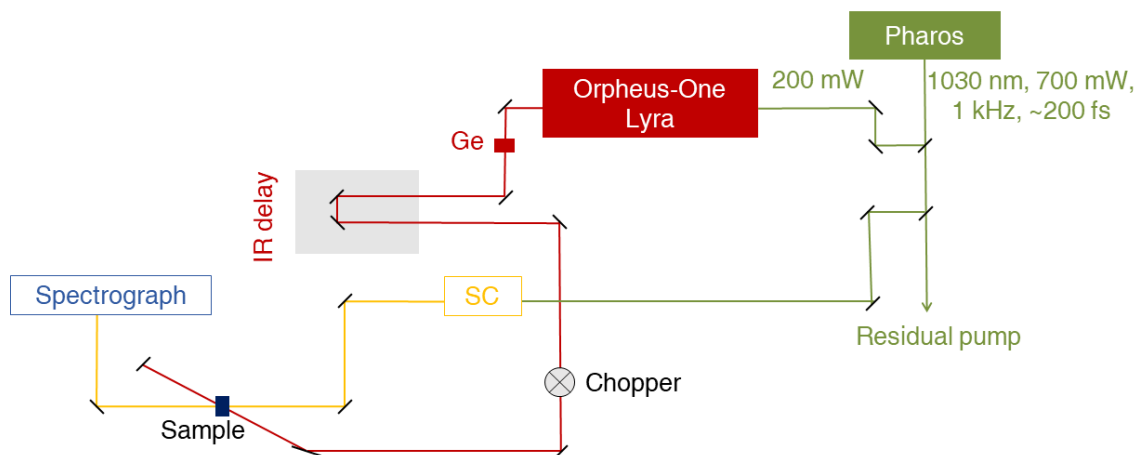
Fig. S1. Schematic of the experimental setup. A commercial femtosecond laser system (Pharos, Light Conversion) is used to drive a commercial optical parametric amplifier (Orpheus-One and Lyra, Light Conversion), which provides the mid-infrared pump laser pulse used in the experiment, after passage through a germanium (Ge) filter, a computer-controlled motorised delay stage and a synchronised optical chopper. The visible probe pulse is generated via supercontinuum generation (SC) in a 2-mm thick sapphire crystal and the transient absorption signal is monitored with a computer-controlled spectrograph (Sciencetech), coupled to a linear CCD image sensor (Hamamatsu).
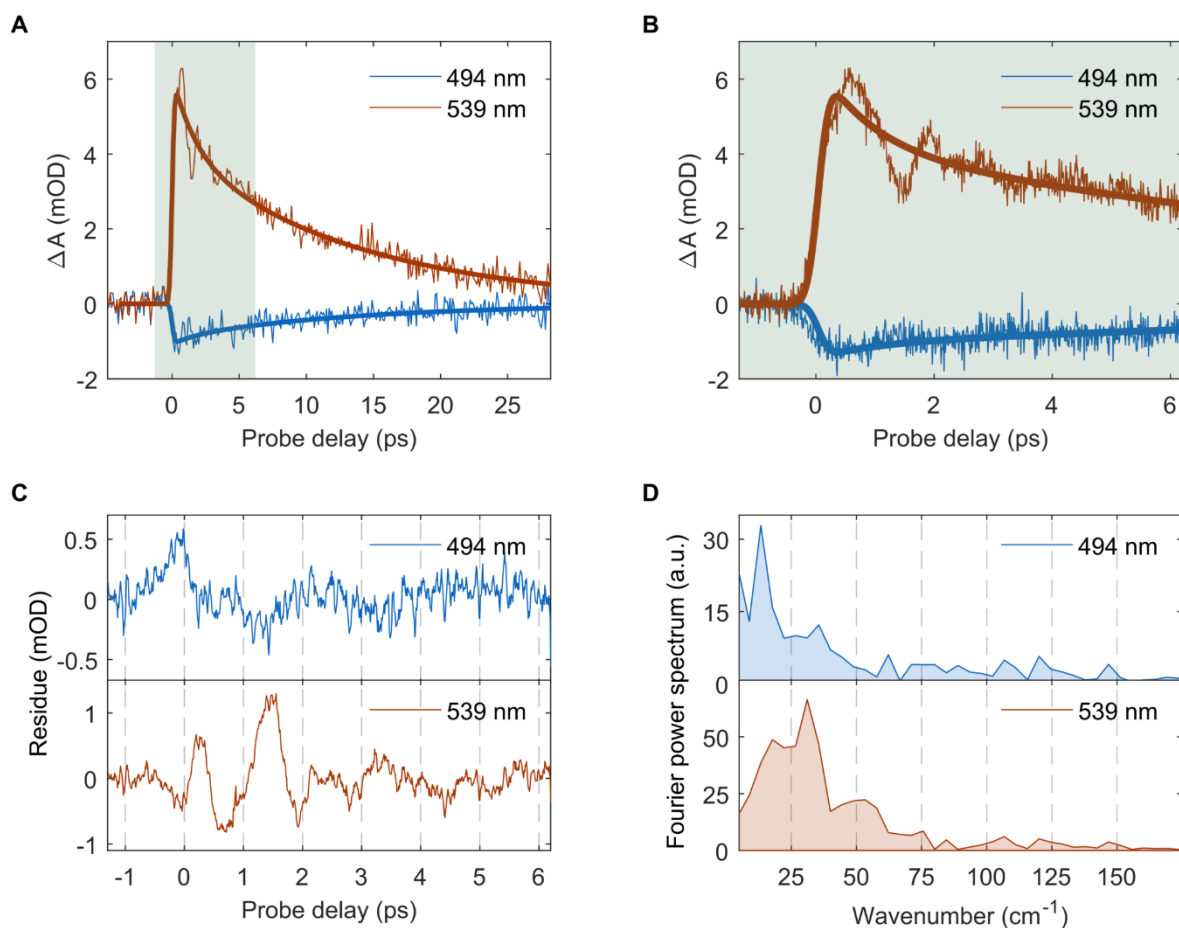
Fig. S2. Time dynamics and frequency analysis of the spectral peaks in the transient absorption measurement. (**A**) Raw experimental transient absorption signal traces (retrieved from Fig. 2A) along with the global-analysis bi-exponential fits for the wavelengths 494 nm and 539 nm, which correspond to the spectral peaks of the negative and positive signals, respectively. (**B**) Analogous results from the high time-resolution experimental run (Fig. 2A), corresponding to the probe-delay range marked by the shaded area in (**A**), providing a magnified view of the temporal oscillations. (**C**) Residual oscillations obtained after removal of the bi-exponential global-fit decay component and (**D**) the corresponding Fourier power spectra for the wavelengths 494 nm and 539 nm, with distinct peaks up to 50 cm^{-1}.
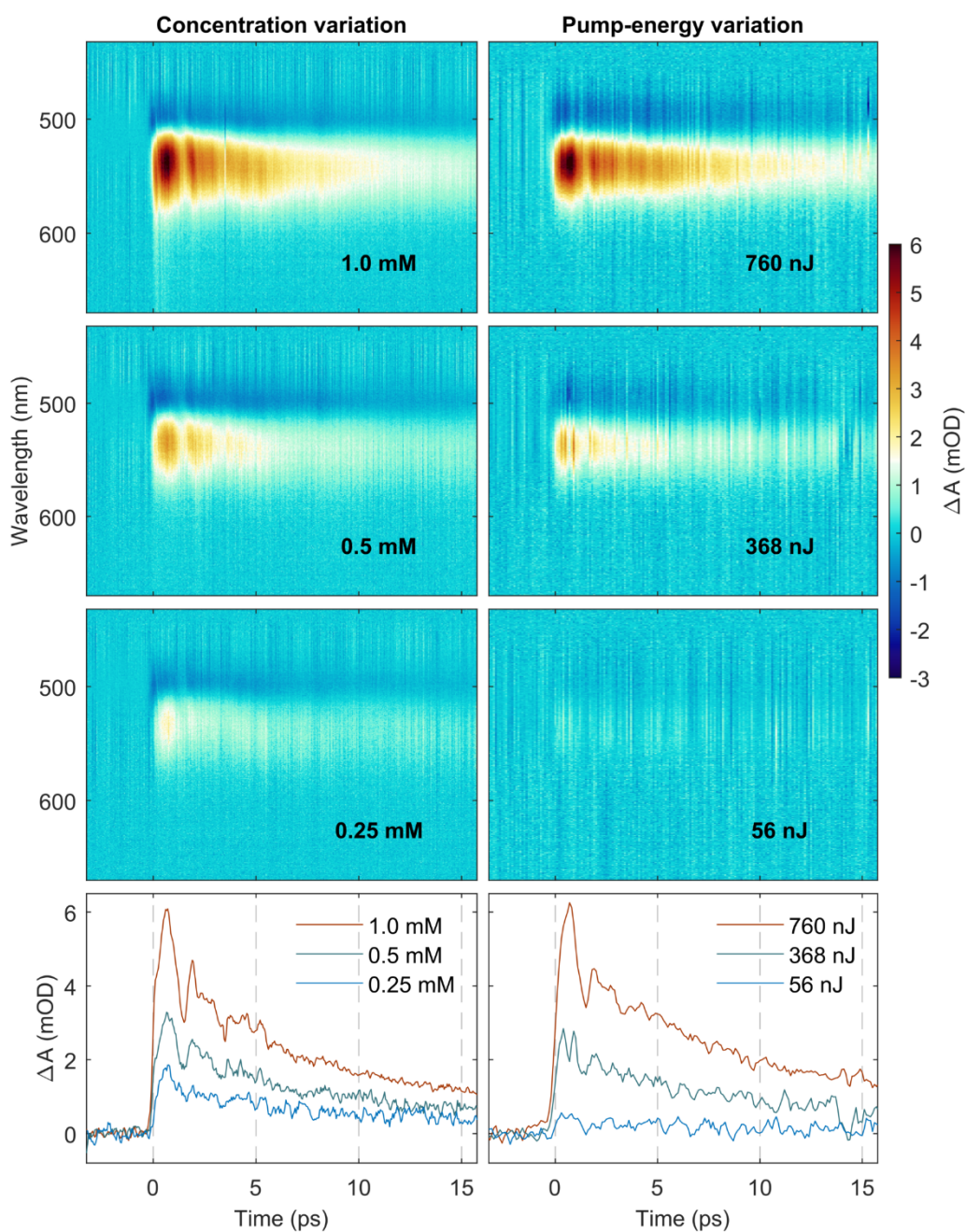
Fig. S3. Effect of the sample concentration and the mid-infrared pump laser energy. Transient absorption signals (top three panels) and spectra at 539 nm (bottom panel) as a function of the concentration of DASPMI in dichloromethane (left panel) and the mid-infrared pump laser energy (right panel). The pump laser energy is attenuated using mid-infrared neutral-density filters (Thorlabs).
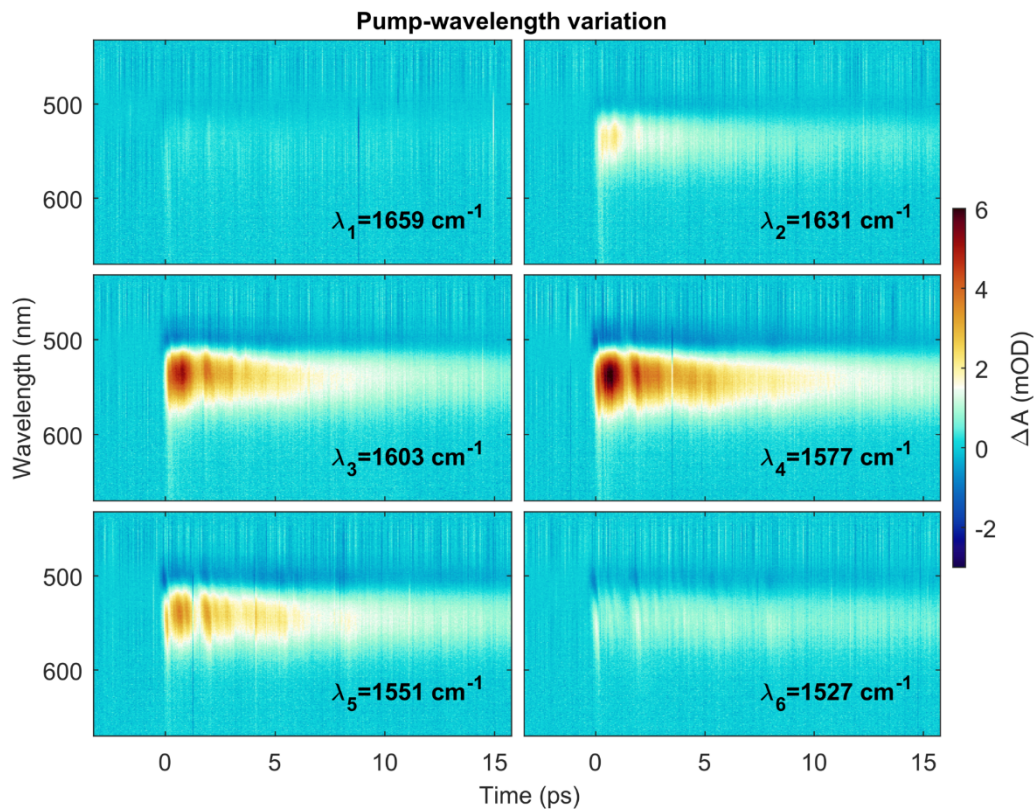
Fig. S4. Effect of tuning the mid-infrared pump laser wavelength. Raw transient absorption signals on varying the central wavelength of the mid-infrared pump laser. The maximum signal corresponds to the resonant mode(s) within the laser spectrum, centred at 1577 cm-1 and with a bandwidth of 50 cm-1.
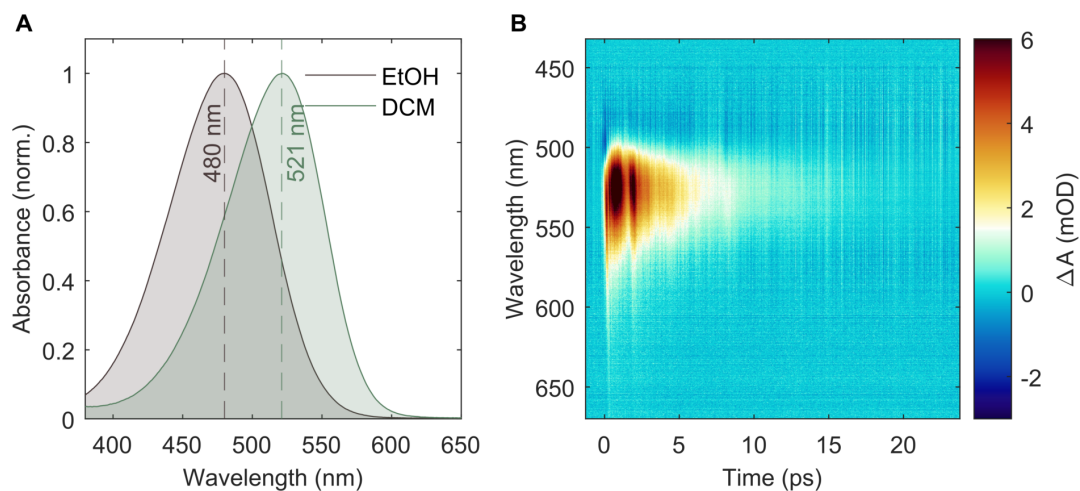
Fig. S5. Transient absorption measurement in ethanol as solvent. (**A**) Steady-state visible absorption spectrum of DASPMI in ethanol (EtOH), and dichloromethane (DCM) for comparison, with absorption peaks at 480 nm and 521 nm, respectively. (**B**) Raw experimental transient absorption signal of a saturated solution of DASPMI in EtOH under otherwise identical experimental conditions in order to investigate the effect of the iodide counter-ion by using a solvent with a different dielectric constant. The negative absorption feature, partially masked but distinctly visible in Fig. 2A, is less conspicuous here due to the blue-shifted absorption in EtOH compared to DCM. However, the transient absorption signal in EtOH shows identical oscillatory dynamics, as observed in DCM.
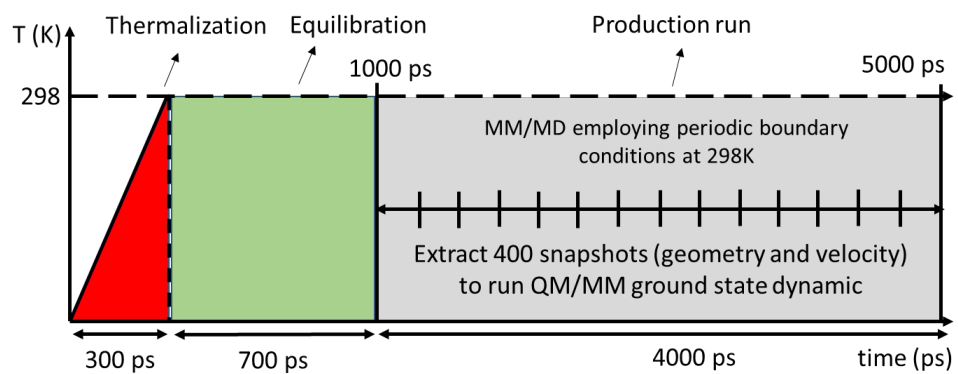
Fig. S6. Schematic of the minimisation steps prior to the QM/MM simulations.
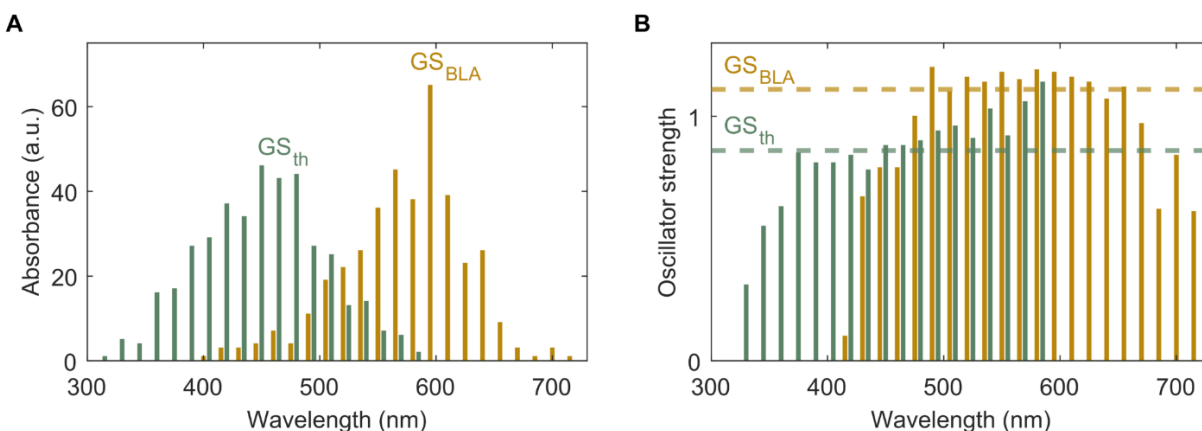
Fig. S7. Simulated absorption spectrum and oscillator strength. Simulation results for 400 trajectories using dichloromethane as solvent. (**A**) The wavelength distribution corresponding to the S_0-S_1 energy gap and (**B**) the corresponding oscillator strength are shown for the initial thermal and the subsequent vibrationally-excited, BLA-activated S_0 populations, GS_{th} and GS_{BLA}, respectively. The theoretical absorption maximum for GS_{th} is localised at 444 nm (64 kcal/mol), which is blue-shifted with respect to the experimental value of 521 nm in the steady-state visible absorption spectrum of DASPMI in dichloromethane (Fig. 1B). This may be attributed to the effect of the counter-ion (iodide) present in the experimental sample solution, which is not included in the simulation model and may cause a red-shifted absorption, in addition to the intrinsic error introduced by the CASPT2//CASSCF protocol (usually ~30-nm blue-shift) [10]. The corresponding oscillator strength, averaged over the entire GS_{th} population, is 0.86 (denoted by the dashed line). For GS_{BLA}, the theoretical absorption maximum for the S_0-S_1 energy gap is red-shifted to 572 nm (50 kcal/mol) and the average oscillator strength increases to 1.11. The increase in the average S_0-S_1 oscillator strength following the creation of the vibrationally-excited, BLA-activated S_0 population may be correlated to the appearance of the transient absorption signal observed experimentally (Fig. 2) with the electronic probe following the vibrational pump.
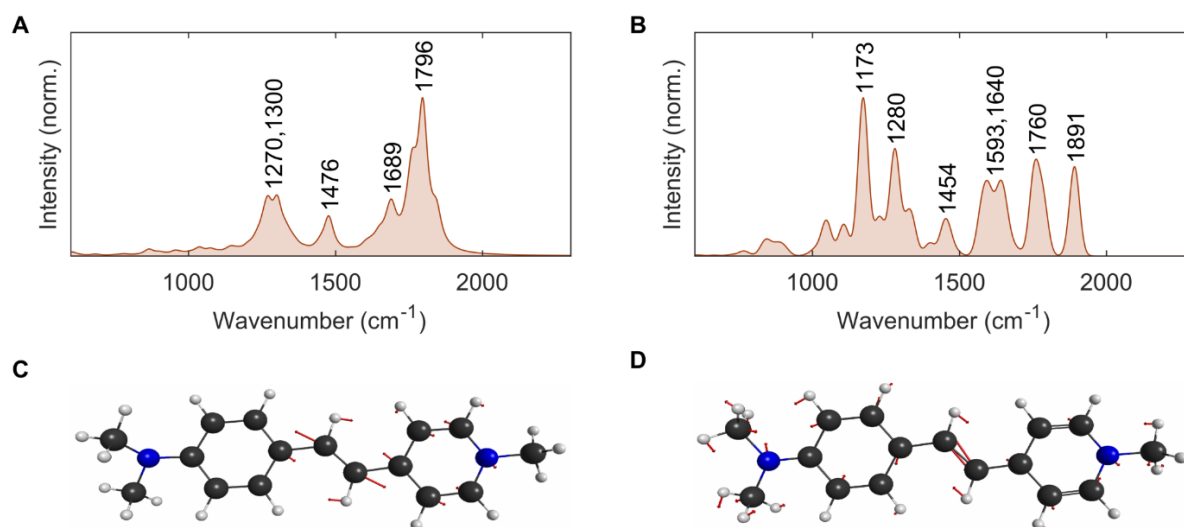
Fig. S8. Vibrational frequency analysis and description of normal modes. Vibrational spectra for the selected geometry optimised on (**A**) S_0 and (**B**) S_1, along with (**C**, **D**) the visualisations of the corresponding normal modes with pronounced BLA character in the vicinity of the central ethylenic bridge. The normal modes depicted correspond to frequencies of (**C**) 1796 cm^{-1} and (**D**) 1173 cm^{-1}, respectively.
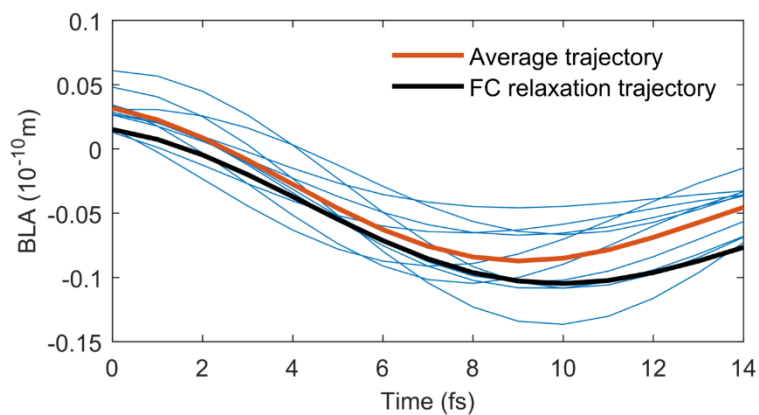
Fig. S9. Excited-state BLA oscillations. S_1 relaxation dynamics for ten randomly selected trajectories from the entire population of 400 trajectories. This S_1 population is created by the projection of the thermal S_0 population onto S_1, conserving positions and momenta. The temporal oscillations along the BLA coordinate, defined as the difference between the average single and double bond-lengths, clearly indicates that energy is released into the BLA mode. The average trajectory (red) shows a maximum at ~9 fs, approximately a quarter of the time-period of the oscillation. For comparison, the Franck-Condon (FC) relaxation trajectory, arising from the vertical transition of the selected S_0-optimised equilibrium geometry to the Franck-Condon point on S_1, is also shown and exhibits a qualitatively similar behaviour.
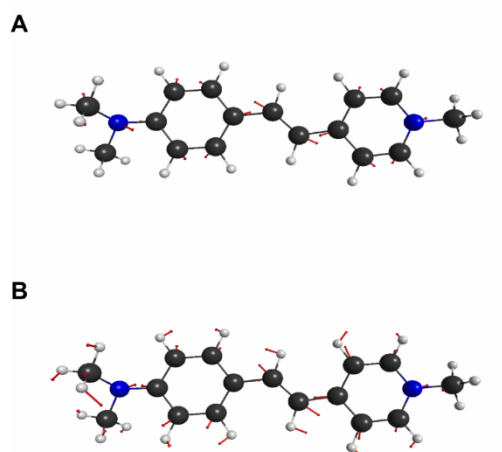
Fig. S10. Visual representations of the evolution of the selected ground-state-optimised equilibrium geometry. (**A**) Snapshot of the direction along which the Franck-Condon relaxation in S_1 occurs at 9 fs. (**B**) Average displacement vector on projection back onto S_0. These may be compared with the normal-mode description in S_0 and S_1 (Fig. S8).
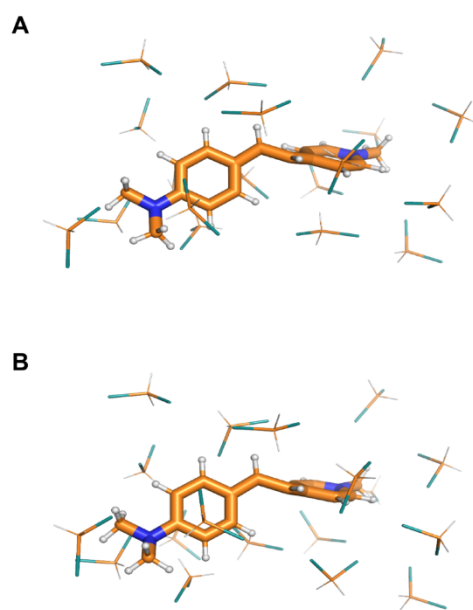
Fig. S11. Optimised geometries. Geometrically similar (**A**) conical intersection (CI) and (**B**) diradical (or covalent) transition state, TS$_{dir}$, configurations, which are located in the vicinity of each other in a rather planar area of S$_0$.
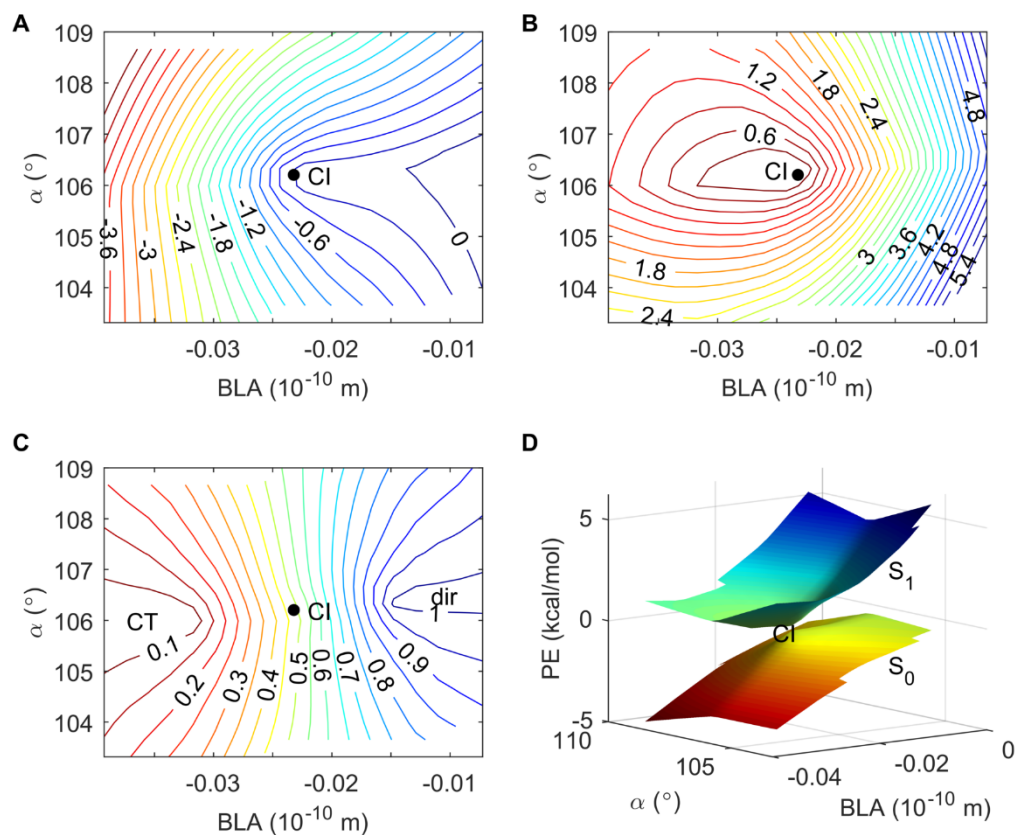
Fig. S12. Potential energy maps and charge-distribution. Potential-energy contour plots from CASSCF calculations, relative to the conical intersection (CI) point (in kcal/mol) for (**A**) S_0 and (**B**) S_1 as a function of the BLA and the torsion, α. (**C**) Contour plot of the S_0 charge-transfer character, ρ, showing the charge-transfer (CT) and the diradical (dir) regions, separated by the CI. (**D**) CI topology.
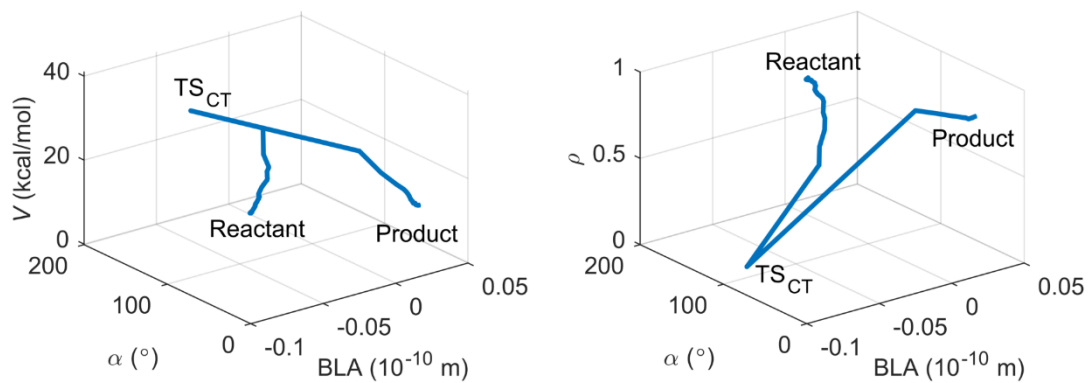
Fig. S13. Minimum-energy path. The minimum-energy path profile for the CASPT2 potential energy, *V*, relative to the reactant and the corresponding charge-transfer character, *ρ.*
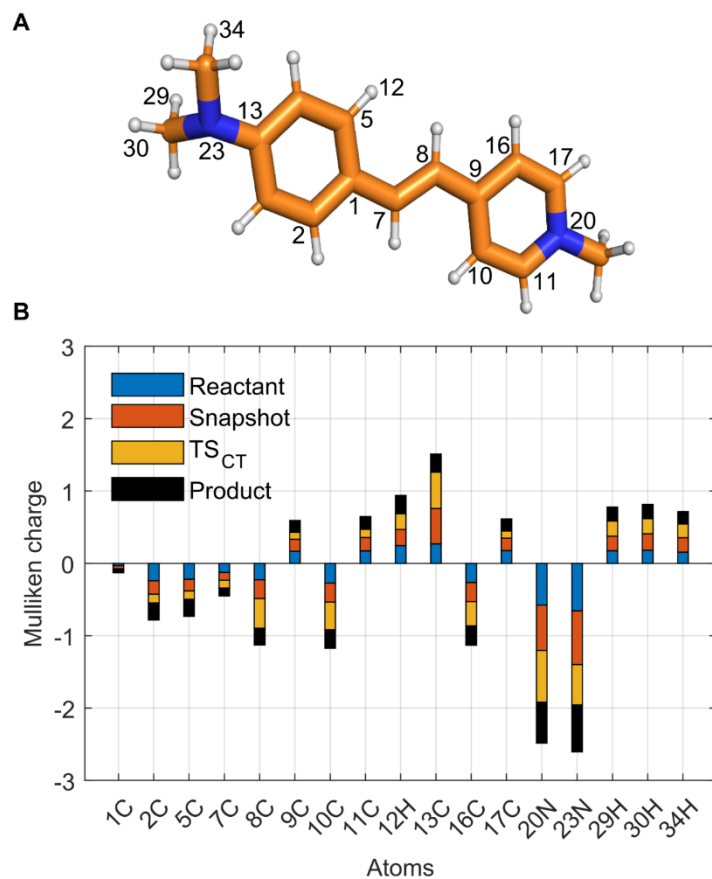
Fig. S14. Mulliken charge distribution analysis. (**A**) The trans-isomer reactant geometry of DASPMI, with certain atoms labelled. (**B**) Mulliken charge distribution for the labelled atoms, for which the difference between the reactant (blue) and TS_{CT} (yellow) is >10%. The variation in the Mulliken charge distribution for a representative snapshot from the trajectory simulations at 1625 fs (red) and the cis-isomer product (black) for these atoms are also shown.
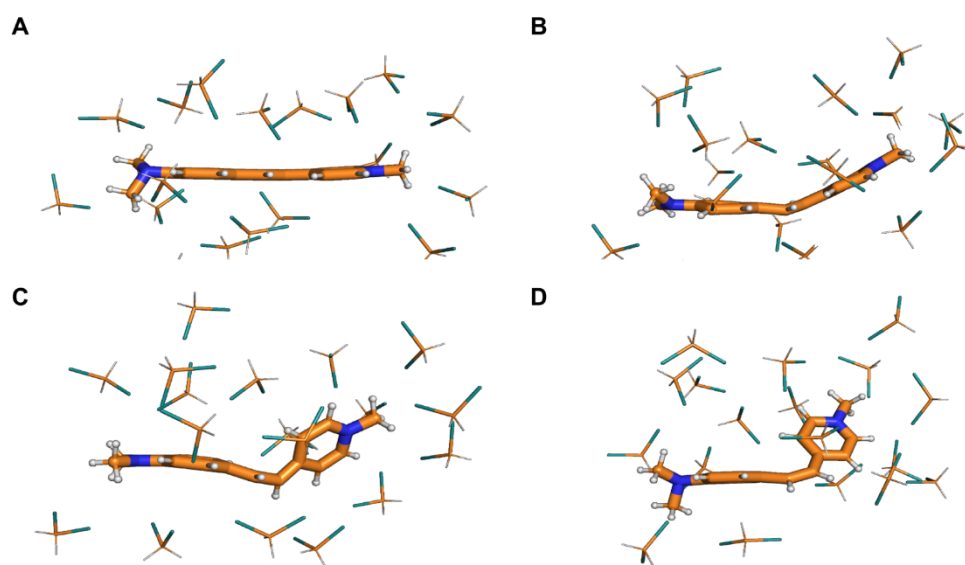
Fig. S15. Visualization of the ground-state isomerization pathway along the molecular plane. Optimised geometries for (**A**) the planar reactant trans-isomer, (**B**) a representative snapshot from one of the 400 trajectories, showing a torsional deformation of ~40^0, (**C**) the highly distorted charge-transfer transition state, TS$_{CT}$, and (**D**) the product cis-isomer.

Table S1: Sensitivity of the S_0-S_1 energy gap to the modes (Fig. S8A) excited by the simulation protocol

Distorted geometries	S_0-S_1 energy gap (kcal/mol)	Difference (kcal/mol)	Difference (%)
S_0 thermalised geometry (reference)	64	0	0
1300 cm^{-1}	60	4	6
1475 cm^{-1}	55	9	14
1796 cm^{-1}	46	18	28
geometry generated via S_1 relaxation	49	15	23

Table S2. ZPE contributions along the vibrational modes associated with the main contributions observed during the Fourier analysis of the trajectories for the three relevant internal coordinates — α, β and BLA.

Frequency (cm^{-1})	Description	ZPE (kcal/mol)
99		0.1
347	Torsion of the central ethylenic bridge, α	0.4
564		0.7
791		1.0
871		1.1
900	HOOP, β	1.2
907		1.2
1075		1.4
1300		1.7
1475	BLA, several stretching modes	1.9
1690		2.2
1796		2.3

References:

[1] S. Miertuš *et al*. Electrostatic interaction of a solute with a continuum. A direct utilization of ab initio molecular potentials for the prevision of solvent effects. *Chem. Phys.* **55,** 117 (1981).

[2] M. Head-Gordon *et al.*, MP2 energy evaluation by direct methods. *Chem. Phys. Lett.* **153,** 503 (1988).

[3] M. J. Frisch *et al.* A direct MP2 gradient method. *Chem. Phys. Lett.* **166,** 275 (1990).

[4] M. J. Frisch *et al.* Gaussian 09, C.01, Gaussian Inc., Wallingford CT, 2016.

[5] C. Caleman *et al.* Force field benchmark of organic liquids: density, enthalpy of vaporization, heat capacities, surface tension, isothermal compressibility, volumetric expansion coefficient, and dielectric constant. *J. Chem. Theory Comput.* **8,** 61 (2012).

[6] S. Pronk *et al.* GROMACS 4.5: A high-throughput and highly parallel open source molecular simulation toolkit. *Bioinformatics* **29,** 845 (2013).

[7] F. Aquilante *et al.* Molcas 8: New capabilities for multiconfigurational quantum chemical calculations across the periodic table. *J. Comput. Chem.* **37,** 506 (2016).

[8] J. W. Ponder & F. M. Richards, TINKER molecular modeling package. *J. Comput. Chem.* **8,** 1016 (1987).

[9] S. Gozem *et al.* Theory and simulation of the ultrafast double-bond isomerization of biological chromophores. *Chem. Rev.* **117,** 13502 (2017).

[10] C. S. Page & M. Olivucci, Ground and excited state CASPT2 geometry optimizations of small organic molecules. J. Comput. Chem. **24,** 298 (2003).